EurJIC
European Journal of Inorganic Chemistry

Research Article
doi.org/10.1002/ejic.202200736

Chemistry Europe
European Chemical Societies Publishing

www.eurjic.org

# How Methylammonium Iodide Reactant Size Affects Morphology and Defect Properties of Mechanochemically Synthesized $MAPbI_3$ Powder

Nico Leupold,[a] Philipp Ramming,[b] Irene Bauer,[b] Christina Witt,[b] Jennifer Jungklaus,[a] Ralf Moos,[a] Helen Grüninger,[c, d] and Fabian Panzer*[b]

Here, we investigate in detail the impact of the size of the methylammonium iodide (MAI) reactants in the mechanochemical powder synthesis of the halide perovskite methylammonium lead iodide ($MAPbI_3$). Morphology and structural characterizations by scanning electron microscopy and X-ray diffraction reveal that with increasing MAI reactant size, the particle size of the perovskite powder increases, while its defect density decreases, as suggested by nuclear quadrupole resonance spectroscopy and photoluminescence investigations. The reason for this behavior seems to be associated to the sensitive influence of the MAI size on the time durations of $MAPbI_3$ synthesis and delayed $MAPbI_3$ crushing stage during ball milling. Thus, our results emphasize the high importance the reactant properties have on the mechanochemical synthesis of halide perovskites and will contribute to enhance the reproducibility and control of the fabrication of halide perovskites in powder form.

## Introduction

Halide perovskites with their $ABX_3$ composition have gained much attention in recent years due to their excellent optoelectronic properties and potential low-cost fabrication. Accordingly, a variety of highly functional optoelectronic devices based on halide perovskites, such as solar cells, light-emitting diodes and detectors for light, X-rays and gamma radiation have been demonstrated.[1]

A key aspect to achieve optimal optoelectronic properties of the perovskite is to ensure a high film quality, which in turn is largely determined by the film fabrication process. To fabricate perovskite films it is possible to process readily synthesized perovskite powders, for example, by powder pressing,[2] powder aerosol deposition,[3] or vapor deposition.[4] Especially in the past few years, these powder-based methods have emerged as a promising alternative to the solvent-based film fabrication methods, where in the latter the reactants (e.g. MAI and $PbI_2$ for the synthesis of $MAPbI_3$) are dissolved and then solution-processed to form the final perovskite film.[5] However, even for classic solvent-based processing routes, redissolving readily synthesized perovskite powders and using these solution for further film processing was demonstrated to exhibit advantages compared to the use of conventional precursor solutions where the individual educts are solved.[6,7] For example, thin films prepared from redissolved powder typically exhibit larger grain size, higher crystallinity, higher phase purity, and lower defect density.[8,9] In addition, the long shelf life[7,10] and increased reproducibility[11] make halide perovskites in powder form attractive for industrial processes.

The powders are usually prepared either by precipitation reactions or by mechanochemical synthesis approaches.[4,8] Here, mechanochemical synthesis has emerged as an attractive route for perovskite powder preparation in recent years, as the stoichiometry can be adjusted very precisely, no solvent is required, and the synthesis can easily be scaled up.[12,13] Besides these technologically relevant advantages, it also became clear that the properties of the final mechanochemically synthesized perovskites depend decisively on the precise synthesis conditions, such as humidity,[9,14] and the feed-in ratio of precursors.[15]

In addition, aspects that are not relevant in solution processing can play a crucial role in the mechanochemical synthesis of halide perovskites. For example, the presence of a liquid milling agent during the mechanochemical synthesis was found to allow for the preparation of formamidinium lead iodide ($FAPbI_3$) in its black perovskite phase with cubic crystal

[a] N. Leupold, J. Jungklaus, Prof. Dr. R. Moos
Department of Functional Materials
University of Bayreuth
Bayreuth 95440 (Germany)
[b] P. Ramming, I. Bauer, C. Witt, Dr. F. Panzer
Soft Matter Optoelectronics
University of Bayreuth
Bayreuth 95440 (Germany)
E-mail: fabian.panzer@uni-bayreuth.de
https://www.ep2-bayreuth.de
[c] Dr. H. Grüninger
Institute for Molecules and Materials
Radboud University
Nijmegen 6525 AJ (The Netherlands)
[d] Dr. H. Grüninger
Northern Bavarian NMR Centre (NBNC) and Inorganic Chemistry
University of Bayreuth
Bayreuth 95440 (Germany)

Supporting information for this article is available on the WWW under https://doi.org/10.1002/ejic.202200736

Research Article
doi.org/10.1002/ejic.202200736



structure, while without milling agent, it was only possible to obtain $FAPbI_3$ in its undesired yellow δ-phase.[9,13] Another aspect that is irrelevant for the solution-based preparation of perovskite films, yet impacts the properties of mechanochemically synthesized perovskite powders is the particle size of the organic and inorganic reactants. While they dissolve in typical precursor solutions, for example, based on DMF or DMSO,[16] the size of the precursor crystals or particles impacts the mechanochemical perovskite synthesis process. As such, the time needed to accomplish a complete mechanochemical synthesis of $MAPbI_3$ decreases with smaller MAI reactant size.[17] While this finding emphasizes the importance of developing a detailed understanding of the influence of MAI reactant size on $MAPbI_3$ powder properties, the exact quantitative influence of MAI reactant size on powder morphology and its optoelectronic properties has not been elucidated yet.

In this work, we investigate in detail how the MAI reactant size affects the morphology, as well as the optical properties of corresponding $MAPbI_3$ powder. For this purpose, we use MAI with three different sizes and mechanochemically synthesize $MAPbI_3$ powder using a planetary ball mill. We characterize the morphology of the synthesized powders by scanning electron microscopy (SEM) and observe structural changes by X-ray diffraction (XRD). Together with nuclear quadrupolar resonance spectroscopy (NQR) and time-resolved photoluminescence (TRPL) measurements, it is possible to correlate the influence of MAI reactant size on the particle size, defect densities and thus the optoelectronic functionality of the mechanochemically synthesized perovskite powders.

## Results

For MAI synthesis, crystalline MAI is precipitated by adding diethyl ether to MAI dissolved in ethanol. Here, the temperature as well as the amount and rate of dropping ether to the MAI-ethanol solution determine the nucleation and growth of the crystalline MAI. Adding a small amount ($<1$ ml) of ether and ensuring slow crystallization by keeping the solution at $-18\,^{\circ}C$ results in crystalline MAI in a rectangular shape with a size ranging from 25 to 1300 μm (mean size 213 μm, hereafter referred to as MAI-large), as extracted from analyses of corresponding SEM images (Figure 1c). Increasing the amount of added ether and increasing the solution temperature to about $0\,^{\circ}C$ yields rectangular MAI with a reduced size in the range of 5 to 44 μm (mean size 16 μm, hereafter referred to as MAI-medium, see also Figure 1b). To produce MAI with smaller particle size, MAI-medium was ground in a planetary ball mill. From the SEM image in Figure 1a (see Figure S1 for higher magnification), it becomes clear that a MAI powder results that consists of agglomerates of primary particles, with a size between 0.1 and 4.1 μm (mean size of 1.1 μm, hereafter referred to as MAI-small). Thus, with the different synthesis procedures, three MAI powders are available with average MAI sizes covering about two orders of magnitude.

Using these three MAI powders, we prepared $MAPbI_3$ in a planetary ball mill. To ensure comparability of the $MAPbI_3$ powders, the amounts of $PbI_2$ and cyclohexane and the milling parameters were kept the same (see experimental section and Figure S1).

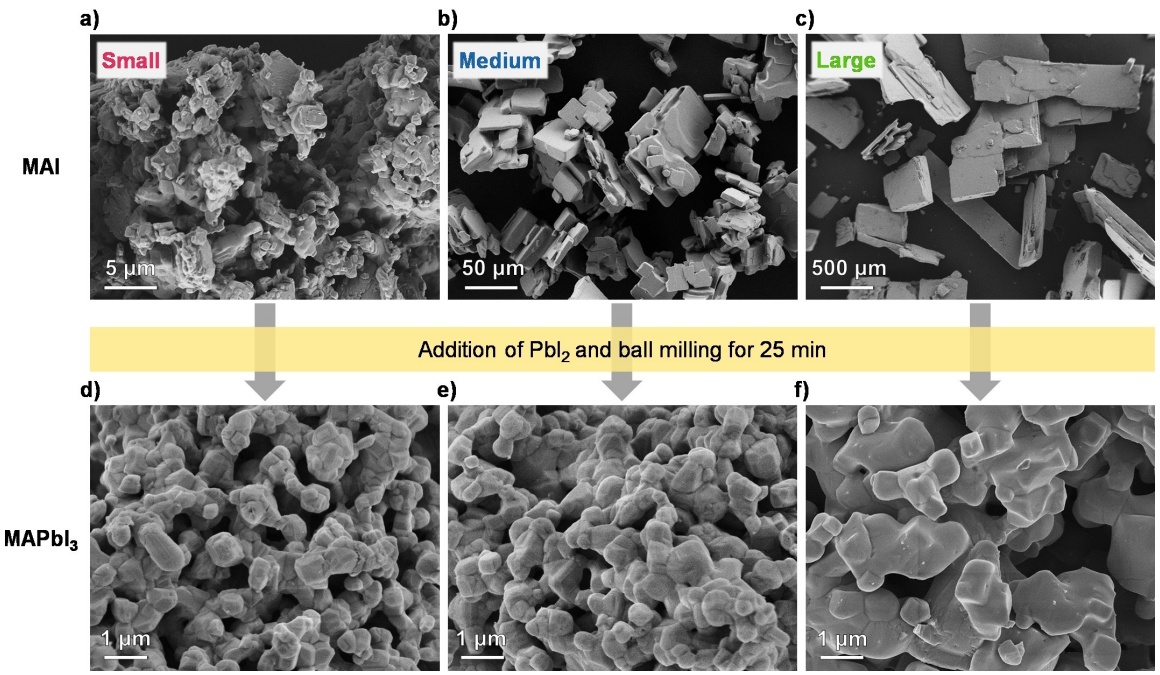


**Figure 1.** Top row: SEM images of the MAI reactant powders with different particle sizes covering two orders of magnitude, referred to as (a) MAI-small, (b) MAI-medium and (c) MAI-large. Bottom row: SEM images of the mechanochemically synthesized $MAPbI_3$ powders resulting from the different MAI reactants. (d) The resulting $MAPbI_3$ powder using MAI-small, (e) resulting $MAPbI_3$ powder using MAI-medium, and (f) resulting $MAPbI_3$ powder using MAI-large.

Research Article
doi.org/10.1002/ejic.202200736



First, we examined the influence of the three different MAI sizes on the morphology of the resulting $MAPbI_3$ powders by SEM (Figure 1d–f). All three $MAPbI_3$ powders are composed of agglomerates, which in turn are composed of primary particles. The average agglomerate size is in the range of 20–30 μm and does not differ significantly between the samples (compare Figure S2). However, it becomes clear from Figure 1d–f that the particle size increases with increasing MAI reactant size.

For a more detailed analysis, we determined the mean particle sizes and the corresponding particle size distribution from the SEM images of the $MAPbI_3$ powders (Figure 2). Specifically, the $MAPbI_3$ particle sizes range from 0.05 to 0.75 μm for $MAPbI_3$ powder synthesized from MAI-small, from 0.15 to 1.05 μm for MAI-medium, and from 0.35 to 1.55 μm for MAI-large (Figure 2a), respectively. Figure 2b shows the mean $MAPbI_3$ particle size and their standard deviation as a measure for the dispersion of the particle sizes resulting from the SEM analyses as a function of MAI reactant size. Here, the mean particle size increases from (0.31 ± 0.13) μm using MAI-small to (0.44 ± 0.17) μm using MAI-medium to (0.68 ± 0.24) μm using MAI-large. Accordingly, the observation of an increase in $MAPbI_3$ particle size with increasing MAI reactant size from the SEM images is also confirmed quantitatively.

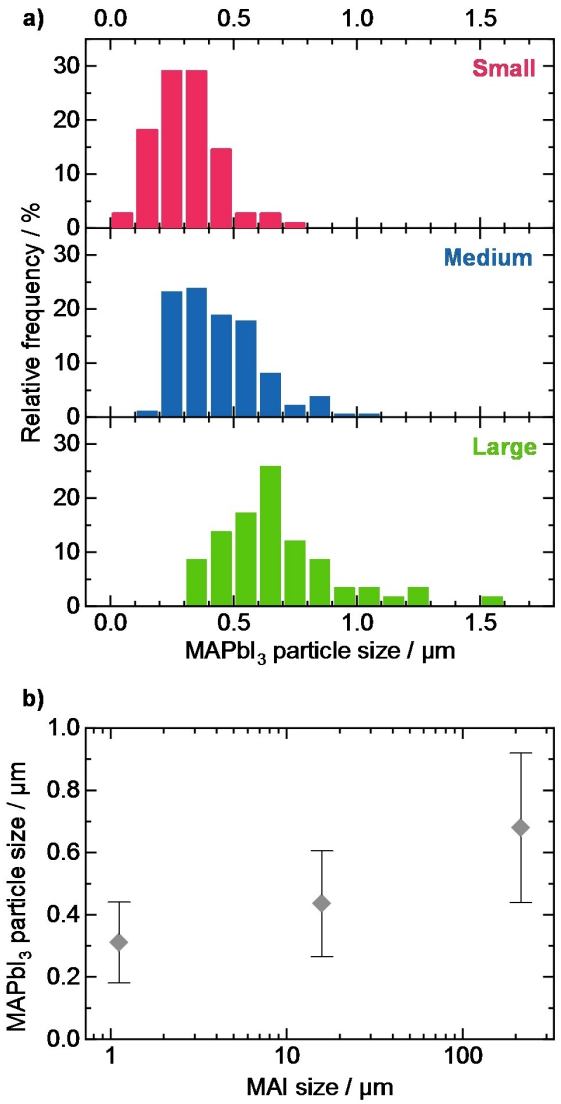


**Figure 2.** (a) Particle size distribution of the resulting $MAPbI_3$ powders using small, medium, and large MAI as reactant. (b) Mean particle size of the resulting $MAPbI_3$ as a function of the MAI reactant size. The bars indicate the standard deviation as a measure for the dispersion of the particle sizes.

To verify that the mechanochemical $MAPbI_3$ synthesis is complete for all three different MAI samples, XRD measurements were conducted. The corresponding diffractograms in Figure 3a show the typical reflections of tetragonal $MAPbI_3$ for all powders (see Figure S3 for indexed diffractograms).[18] Also, no reflections that are associated with crystalline $PbI_2$ reactant (e.g., at $2\Theta = 12.6°$) are found in the diffractograms,[19] suggesting complete synthesis of all three $MAPbI_3$ powders despite the different MAI sizes and morphologies. This is further supported by $^{207}Pb$ NMR measurements of the three $MAPbI_3$ powders (Figure S4), where alone the signal for $MAPbI_3$ at a chemical shift of about 1430 ppm and no signals corresponding to $PbI_2$ phase at a chemical shift between 0 and −30 ppm were detected.[20] Furthermore, the NMR intensities of all samples normalized to the largest integrated intensity under consideration of the sample mass are about unity, which strongly suggests the absence of impurity phases.

By considering the width of the reflections in the XRD patterns (Figure 3a), it is possible to gain insights about the influence of MAI reactant size on the $MAPbI_3$ crystallite size and microstrain. To this end, we fitted Pseudo-Voigt functions to the (220)-reflections at $2\Theta = 28.5°$ and extracted the corresponding full-width at half maximum (FWHM) for the $MAPbI_3$ powders produced from different MAI sizes. From this analysis, it becomes clear that the FWHM of the (220)-reflections decreases with increasing MAI reactant size from 0.053° using MAI-small, to 0.051° using MAI-medium, to 0.045° using MAI-large (Figure 3b). A decrease in FWHM typically results from a decrease in microstrain and/or an increase in crystallite size.[21] Both are strongly related to defects like grain boundaries, crystal twinning, the particle surface, orientation misfits, dislocations, and point defects, as defects may disturb the coherently scattering domains (crystallite size) and induce local variations in the lattice spacing (microstrain).[21–23] As the extracted FWHM of the powders is close to the instrumental resolution of (0.0423 ± 0.0003)°, we did not extract the microstrain and crystallite size quantitatively, for example, by applying Williamson-Hall analysis, but focus on the FWHM. The decreasing FWHM with increasing MAI reactant size indicates that the resulting $MAPbI_3$ powders exhibit less microstrain and/or larger crystallites and thus a more uniform crystal lattice that is less disturbed by defects.

To confirm this correlation, we performed $^{127}I$ nuclear quadrupole resonance (NQR) measurements on the three $MAPbI_3$ powders (Figure 3c). The spectra show two peaks for the 3/2→5/2 spin transition for each $MAPbI_3$ powder as there are two different positions for the iodide (unequal axial and equatorial I ions) in the tetragonal crystal lattice.[24] Here, the FWHM of the peak at 164.1 MHz in the spectrum shows a decrease from 56.3 kHz (small) to 54.3 kHz (medium) and

Research Article
doi.org/10.1002/ejic.202200736



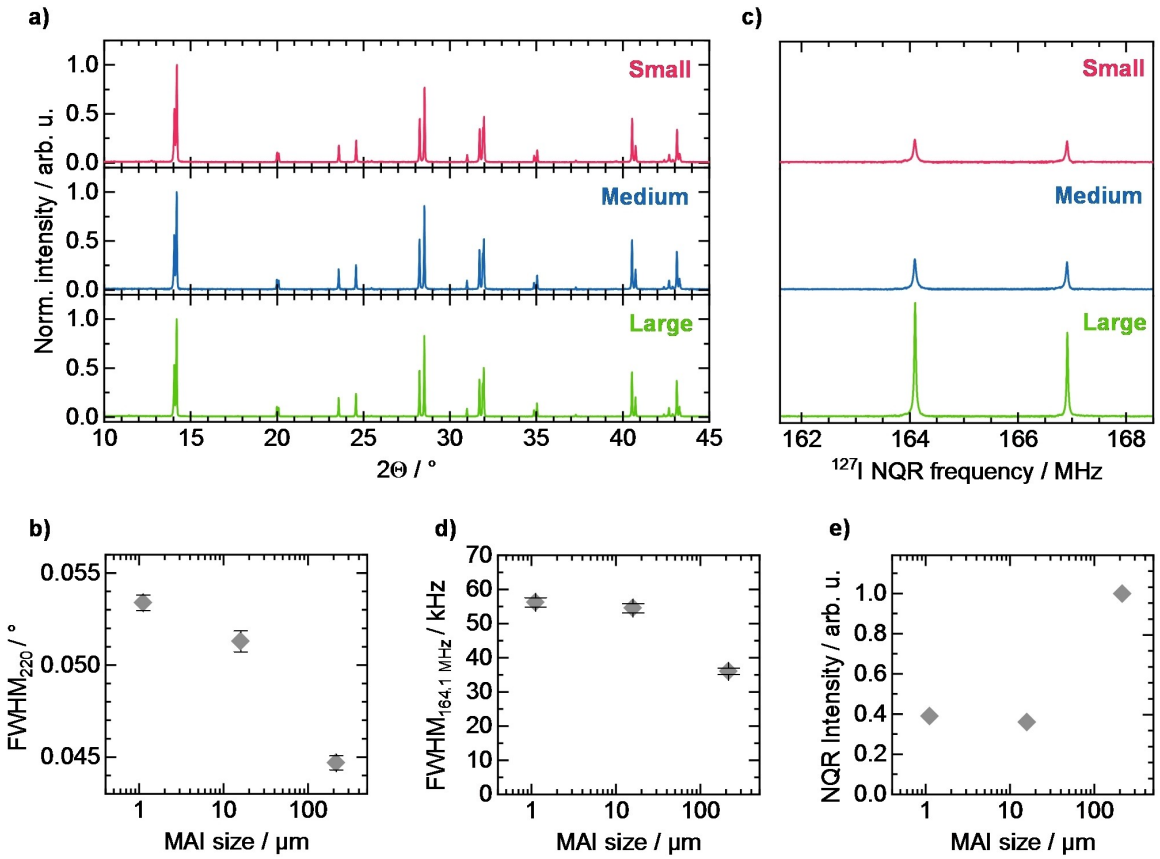


**Figure 3.** (a) XRD patterns of $MAPbI_3$ powders synthesized with different MAI sizes. (b) FWHM of the (220) reflection from XRD measurement as a function of the MAI reactant size. (c) $^{127}I$ NQR measurement of $MAPbI_3$ powders synthesized with different MAI sizes. (d) FWHM of the Peak at 164.1 MHz and (e) sum of the integrated intensity of both Peaks from the $^{127}I$ NQR measurements as a function of the MAI size. The sum of the integrated intensity was divided by the sample mass to correct for small differences in the sample mass and normalized to the integrated intensity of the $MAPbI_3$ powder from MAI-large.

36.1 kHz (large) for increasing MAI reactant size (Figure 3d), while the integrated peak intensity under consideration of the respective sample mass increases (Figure 3e). Analogously, also the FWHM of the peak at 166.9 Hz decreases with increasing MAI reactant size (Figure S5).

In general, $^{127}I$ NQR measurements are sensitive to the local structural environments of the iodide in the halide perovskite crystal lattice and are influenced by the chemical composition and by, for example, microstrain and resulting distortions.[25] Consequently, if the ions surrounding the iodide are arranged uniformly (i.e., ordered) in the sample, narrow peaks result.[26] In contrast, defects change the associated iodide environments and induce distortions in the next-neighbor coordination shells, which in the case of $MAPbI_3$ was found to lead to peak broadening and to a reduction of the integrated signal intensity.[27] Thus, the decrease in FWHM and simultaneous increase in intensity observed in Figure 3 indicates that the iodide environment in the $MAPbI_3$ powder is less disturbed by defects with increasing MAI reactant size. From the decrease in FWHM of the reflections in XRD and peaks in NQR and from the increase in NQR intensity with increasing MAI reactant size, we conclude that the defect density in the synthesized $MAPbI_3$ powder decreases with increasing MAI reactant size.

To investigate how the observed differences in defect density in the $MAPbI_3$ powders affect their optical and excited state properties, we performed time-resolved photoluminescence (TRPL). Figure 4a shows the spectra of the time-integrated PL decay curves of the three perovskite powders. All spectra exhibit the typical PL peak for $MAPbI_3$ with a maximum at about 770 nm (Figure 4a and Figure S6).[28] In contrast, the PL intensities of the different $MAPbI_3$ powders deviate from each other, with $MAPbI_3$ made from MAI-large showing the lowest, from MAI-small showing a medium, and from MAI-medium showing the highest intensity (Figure 4a).

The normalized PL decay curves of the three $MAPbI_3$ powders exhibit a similar behavior, i.e., dropping to about $10^{-3}$ of their original PL intensity after a time $t$ of 400 ns after the laser excitation (Figure 4b). In halide perovskites, the PL decay can be described with the rate Equation (1):[29]

$$-\frac{dn}{dt} = k_1 n + k_2 n^2 + k_3 n^3 \quad (1)$$

In this equation, $n$ is the charge carrier density, $t$ denotes the time, $k_1$ is the rate constant for the nonradiative monomolecular recombination, $k_2$ the rate constant for radiative

Research Article
doi.org/10.1002/ejic.202200736



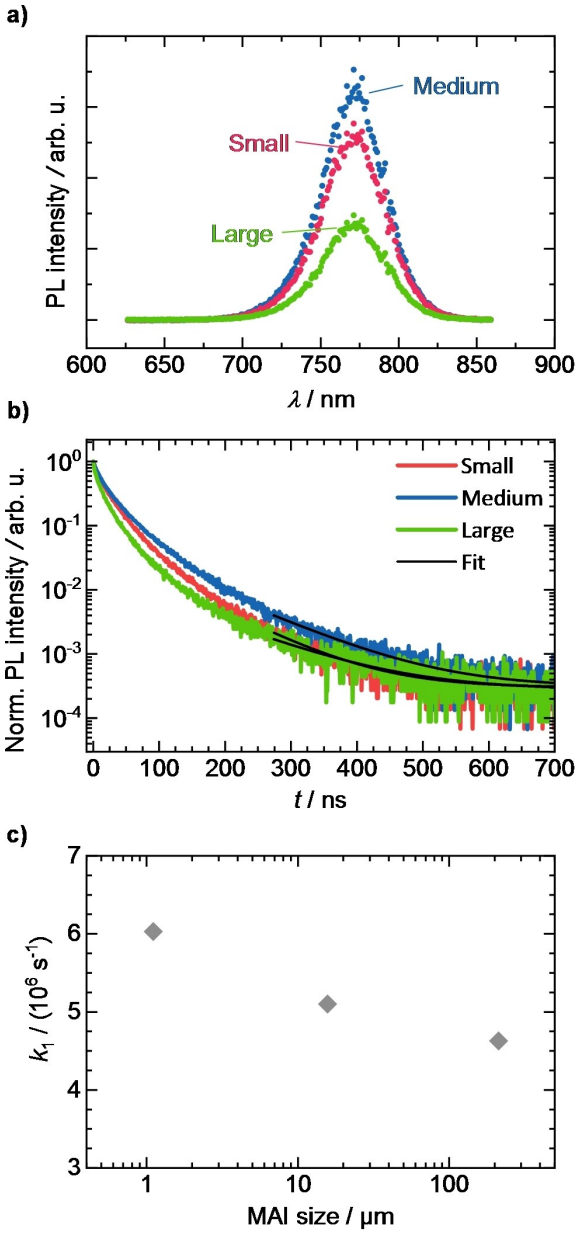


**Figure 4.** (a) PL spectra of the $MAPbI_3$ powders synthesized with different MAI reactant sizes. (b) Normalized time-resolved PL (TRPL) measurements of $MAPbI_3$ powders synthesized with different MAI reactant sizes together with exponential tail fits (black lines) as described in the text. (c) Rate constants $k_1$ extracted from the TRPL analyses as a function of MAI reactant size.

band-to-band recombination, and $k_3$ the rate constant for Auger recombination. At longer times, when the charge carrier density is low, the measured PL decay is thus dominated by the monomolecular recombination of the photoinduced charge carriers.[30] In particular, this nonradiative recombination channel has been associated with the recombination of charge carriers at defects (Shockley-Read-Hall recombination).[31] Hence, quantification of the monomolecular recombination rate $k_1$ allows to draw conclusions about the defect density within the perovskite. Using the relationship[32] (Eq. (2))

$$PL(t) \sim \exp(-2 \times k_1 \times t) \quad (2)$$

and considering the dark counts of the detector as a baseline, we quantify $k_1$, by fitting a monoexponential function to the measured PL decay curves for times longer than 275 ns (see solid lines in Figure 4b). From this analysis, we find the recombination rate $k_1$ of the $MAPbI_3$ powders to decrease from $6.0 \times 10^6\ s^{-1}$ (MAI-small) to $5.1 \times 10^6\ s^{-1}$ (MAI-medium) to $4.6 \times 10^6\ s^{-1}$ (MAI-large) with increasing MAI reactant size (Figure 4c). The decreasing monomolecular recombination rate with increasing MAI reactant size (or particle size of the final $MAPbI_3$ powder respectively), again indicates a decreasing defect density in the larger sized perovskite powder, in agreement with the results from the XRD and NQR analyses.

In general, under constant measurement conditions, a reduction in defect density and thus $k_1$ in halide perovskites leads to an increase in their measured PL intensity as the PL quantum yield $\Phi$ is proportional to[30,32,33] (Eq. (3))

$$\Phi \sim \frac{k_2 n}{k_1 + k_2 n + k_3 n^2} \quad (3)$$

This is consistent with the PL intensity of the $MAPbI_3$ powder made from MAI-small being lower than the intensity of the powder made from MAI-medium (Figure 4a). However, the fact that the perovskite powder made from MAI-large exhibits the lowest PL intensity even though this sample has the lowest $k_1$ value appears surprising. While a detailed investigation of the origin of this behavior is beyond the scope of this work, we speculate that due to the larger average particle size in the perovskite powder made from MAI-large (compared to the other two powders) a more pronounced charge carrier diffusion after photoexcitation is present. This is consistent with the initial PL decay of the powder large being faster than for the other two powders as is noticeable in Figure 4b. A more pronounced diffusion leads to an overall lower charge carrier density during recombination, which according to equation (3) results in a lower PL intensity. A similar effect was observed for thin films, where the PL intensity of large grains was significantly reduced compared to small grains of the same film.[34]

## Discussion

In the following, we first summarize the findings about the mechanism and possible pathways of mechanochemical synthesis of halide perovskites that have been published in the past, before discussing our results in the context of the literature findings.

Manukyan et al. studied the mechanochemical synthesis of MAI and $PbI_2$ to $MAPbI_3$ and concluded that during the mechanochemical synthesis the MAI plastically deforms, creating cracks and pores in the MAI particles. $PbI_2$, on the other hand, is brittle, so it is mainly crushed during synthesis.[35] In addition, the $PbI_2$ is forced into the MAI during synthesis, so

Research Article
doi.org/10.1002/ejic.202200736





that both MAI and $PbI_2$ are in close contact, which enables the interdiffusion of MAI and $PbI_2$. Here, an increased surface area of the $PbI_2$ reactant (given for lower $PbI_2$ reactant sizes) enhances and accelerates the interdiffusion. The introduced mechanical energy is also expected to create point defects and dislocations in the reactants.[35,36] The presence of such defects facilitates the interdiffusion of MAI and $PbI_2$.[36,37] As the Gibbs free energy to form $MAPbI_3$ from MAI and $PbI_2$ is negative at room temperature, a facilitated reactant interdiffusion also fosters the subsequent perovskite reaction.[38] This is consistent with the Study of Gil-Gonzáles et al. on the mechanochemical synthesis of $MAPbCl_3$, where the authors find a steep increase in the fraction of formed perovskite at the beginning of the synthesis. This slows down at a later stage of the mechanochemical synthesis process, as the diffusion paths become longer and the probability of unreacted $PbI_2$ encountering MAI decreases.[39]

The sequence of the mechanochemical synthesis was also studied in detail by Palazon et al. using $CsPbBr_3$. Here, three distinct synthesis stages could be identified.[22] In the first stage, which extended over the first 5 minutes, the reactants CsBr and $PbBr_2$ form $CsPbBr_3$, as well as non-stoichiometric intermediate phases. These intermediate phases and remaining reactants completely convert into $CsPbBr_3$ in the second stage. After the complete conversion to perovskite, the $CsPbBr_3$ powder gets crushed in a third stage, which is accompanied by a decrease in crystallite size. This also leads to a general trend of decreasing PL intensity with longer milling times, although the trend is interrupted at some milling times where the PL intensity is larger for the longer milling time than at the time before, indicating a more complex relationship between the PL intensity and the milling time. In a previous work, we also observed a decrease in particle size with increasing milling time after complete mechanochemical synthesis of $MAPbI_3$.[17] Overall, it thus becomes clear that in the mechanochemical synthesis of halide perovskites via ball milling, an initial synthesis stage, in which the perovskite forms, is followed by a stage of crushing the perovskite powder.

The insights from literature can be transferred to our results to understand the influence of MAI reactant size on the properties of the synthesized $MAPbI_3$ powders. The larger the MAI reactant powder, the more energy is required for plastic deformation and the introduction of defects during the synthesis stage. Also, more energy is required to crush the MAI, increasing the general diffusion lengths for perovskite formation. As a consequence, the initial perovskite synthesis stage is longer for increasing MAI reactant size. During the synthesis, from a certain point onwards, the crushing stage of the synthesized $MAPbI_3$ starts, during which the perovskite particle and crystallite size decreases.[17,22] For a constant overall milling time (as it is the case in the present study), a reduction of the duration of the initial perovskite synthesis stage for smaller MAI reactant size goes along with an extension of the crushing stage duration. Prolonged dwelling in the crushing stage results in final perovskite powders that exhibit a reduced particle size (Figure 2b), increased defect density (Figure 3d), and an increased non-radiative decay rate of excited states (Figure 4c), fully in line with our experimental results.

## Conclusion

By detailed characterization of $MAPbI_3$ powders, mechanochemically synthesized from MAI of different sizes, we identified a clear influence of the MAI reactant size on the final $MAPbI_3$ powder properties. In particular, with increasing MAI reactant size, we observed an increase in particle size in the perovskite powder as deduced from SEM images. The increase in particle size is accompanied by a decrease in defect density in the $MAPbI_3$ powder, which was inferred from NQR and TRPL analyses.

Our results thus emphasize the importance for precise control of the organohalide reactant size to ensure a reproducible, well-defined perovskite powder morphology and optoelectronic functionality. The precise properties of perovskite powders are known to directly impact the properties of films that are made from these powders, for example, via pressing, powder aerosol deposition, or suspension deposition.[4] Consequently, our results will contribute to advance the development of efficient perovskite powder-based optoelectronic devices in the future.

## Experimental Section

**MAI synthesis**: 20 mL of methylamine (160 mmol, 33 wt% in ethanol, Sigma Aldrich) were dissolved in 170 mL of ethanol under argon atmosphere. Then, 22.18 mL (168 mmol) of HI (57 wt% in $H_2O$, Alfa Aesar) were added dropwise under constant stirring within 30 min, while the solution was cooled with an ice bath. After stirring the solution overnight, the solvent was removed by a rotary evaporator and the powder was washed with a diethyl ether-ethanol mixture. In the final step, the powder was again dissolved in 50 ml ethanol and 250 ml diethyl ether were dropped into the concentrated solution of MAI at room temperature to crystallize the final white MAI powder. In this step, the rate of ether addition determines the crystallization rate and thus the MAI size. The ether was added within 1 to 2 min, after which the MAI was separated by filtration and washed with diethyl ether. The process of redissolution and crystallization was repeated before the MAI powder was dried. The resulting powder was called MAI-medium.

To prepare MAI-large, 5 g MAI-medium were dissolved in 25 ml ethanol and a few drops ($<1$ ml) of diethyl ether were added. Slow crystallization was first carried out in a refrigerator at 7 °C for 5 h and then in a freezer at −18 °C overnight. Finally, the powder was filtered and dried. To obtain MAI-small, 5.5 g of MAI-medium were milled in the planetary ball mill using the same procedure as for the mechanochemical synthesis.

**Mechanochemical synthesis**: For the mechanochemical synthesis of $MAPbI_3$, 1.55 g of the respective MAI reactant powders and 4.5 g of $PbI_2$ (99.99%, TCI) were added to 80 ml $ZrO_2$ milling jars together with 5 mL cyclohexane and 25 $ZrO_2$ milling balls with a diameter of 10 mm. During weighing-in, the relative humidity was about 45% at a temperature of 21 to 25 °C. A Fritsch "Pulverisette 5/4" planetary ball mill with 400 rpm was used for synthesis. After 5 min of milling, a pause of 20 min was implemented to prevent excessive heating of the milling jar. The process was repeated until a total

milling time of 25 min was achieved. Afterwards, the cyclohexane was evaporated in air and the obtained black $MAPbI_3$ powder was sieved using a mesh size of 63 μm.

**Sample Characterization**: For morphology studies, SEM images of the perovskite and MAI powders were taken with a Zeiss Leo 1530 scanning electron microscope (FE-SEM with Schottky-field-emission cathode, SE2 detector and In-lens detector) using an accelerating voltage of 3.0 kV. The powders were fixed on a sample holder with conductive graphite pads (Plano) and sputtered with a 1.5 nm thin platinum layer. To calculate the area of the MAI particles, their lengths and widths were determined manually using the SEM images. The MAI size was then recalculated as the equivalent edge length of a square with the same area. For MAI-small 53 particles, for MAI-medium 54 particles, and for MAI-large 39 particles were used to calculate the average size. The particle size of the $MAPbI_3$ powders was determined from SEM images. Here, the particle boundaries were manually retraced before the area of each particle was calculated using imageJ. The particle size was then calculated from the area of the particles as the equivalent diameter of a circle with the same area. The average particle size and the standard deviation as a parameter for dispersion were obtained using 110 particles for the $MAPbI_3$ powder made from MAI-small, 185 for the $MAPbI_3$ powder made from MAI-medium, and 58 for the $MAPbI_3$ powder made from MAI-large.

XRD patterns were acquired under ambient conditions by reflection mode XRD using a Bruker "D8 Discover A25" with Cu-$K_{\alpha 1}$ radiation ($\lambda = 0.15406$ nm) and Ge-$K_{\alpha 1}$ monochromator. The X-ray source was operated with 40 kV and 40 mA. Diffractograms were recorded with a $2\theta$ step size of 0.008° in the $2\theta$ range from 10° to 45°. To determine the instrumental resolution and the measurement error, a standard alumina sample (SRM 1976c, provided by Bruker) was measured 6 times and the FWHM was determined by fitting a Pseudo-Voigt function to the (104)-reflex.

$^{127}I$ NQR spectra (3/2→5/2) were recorded on a 300 MHz Varian V NMRS system with a Varian 3.2 mm T3 HXY probe head placed far away from the magnet. The NQR frequencies were 164.1 and 166.9 MHz (3/2→5/2) at room temperature. As the $T_1$ relaxation was extremely short (~30 μs) a fast recycle delay was used (0.1 s) with 8192 scans using a Hahn-echo experiment with as short delays as possible. $^{207}Pb$ MAS NMR spectra were recorded on Varian V NMRS systems operating at a magnetic field strength of 14.1 T using a Varian 3.2 mm T3 HXY probe head at room temperature. The $^{207}Pb$ MAS NMR spectra were recorded at 5 kHz spinning speed with a recycle delay of 0.5 s. The chemical shift was referenced using lead nitrate for $^{207}Pb$ (−3494 ppm) as secondary reference.

Time-resolved PL measurements of the perovskite powders were recorded using time-correlated single-photon counting (TCSPC) on a PicoQuant MT200 confocal fluorescence microscope. Excitation was performed using a 560 nm diode laser (PicoQuant LDH-D-TA-560) at a frequency of 1.0 MHz, with a pulse width of 68 ps, and a fluence of about 100 $nJ/cm^2$. The laser light was focused on the powder sample with an Olympus objective (4× magnification, numerical aperture of 0.1). The emitted light was filtered with a 561 nm long pass filter and detected with a PMA Hybrid PMT 40 photomultiplier tube (PicoQuant). The Signal was processed using a Picoquant TimeHarp 260 Pico TCPSC board. The PL spectra were also acquired with this setup using a Shamrock SR163 spectrograph and a Newton 970 EMCCD camera (Andor).

## Acknowledgements

*The authors acknowledge financial support by the Deutsche Forschungsgemeinschaft (DFG, German Research Foundation) via the projects PA 3373/3-1, MO 1060/32-1, GR 5505/1-1 and 506642499. We further thank the Department of Metal and Alloys (Prof. Uwe Glatzel) of the University of Bayreuth for the possibility to conduct XRD measurements and Angelika Mergner, Nicole Hall and the KeyLab Electron and Optical Microscopy of the Bavarian Polymer Institute (BPI) for SEM images and access to the MT200 confocal fluorescence microscope. H.G. thanks NWO for the support of the "Solid-State NMR Facilities for Advanced Materials Science", which is part of the uNMR-NL ROADMAP facility (grant nr. 184.035.002) and the MRRC facility technicians Gerrit Janssen, Hans Janssen, and Ruud Aspers for their support. Also, we thank Dr. rer. nat. Konstantin Schötz for fruitful discussions. Open Access funding enabled and organized by Projekt DEAL.*

## Conflict of Interest

The authors declare no conflict of interest.

## Data Availability Statement

The data that support the findings of this study are available from the corresponding author upon reasonable request.

**Keywords:** Ball milling · Lead halide perovskites · Methylammonium lead iodide · Optical properties · Semiconductors

[1] a) M. Ahmadi, T. Wu, B. Hu, *Adv. Mater.* **2017**, *29*, 1605242; b) K. Ji, M. Anaya, A. Abfalterer, S. D. Stranks, *Adv. Opt. Mater.* **2021**, 2002128; c) G. Kakavelakis, M. Gedda, A. Panagiotopoulos, E. Kymakis, T. D. Anthopoulos, K. Petridis, *Adv. Sci.* **2020**, *7*, 2002098; d) NREL, "Research Cell Record Efficiency Chart", can be found under https://www.nrel.gov/pv/cell-efficiency.html.
[2] C. Witt, A. Schmid, N. Leupold, M. Schultz, J. Höcker, A. Baumann, R. Moos, F. Panzer, *ACS Appl. Electron. Mater.* **2020**, *2*, 2619.
[3] M. Schubert, D. Hanft, T. Nazarenus, J. Exner, M. Schubert, P. Nieke, P. Glosse, N. Leupold, J. Kita, R. Moos, *Funct. Mater. Lett.* **2019**, *12*, 1930005.
[4] N. Leupold, F. Panzer, *Adv. Funct. Mater.* **2021**, *31*, 2007350.
[5] W. A. Dunlap-Shohl, Y. Zhou, N. P. Padture, D. B. Mitzi, *Chem. Rev.* **2019**, *119*, 3193.
[6] D. Prochowicz, P. Yadav, M. Saliba, M. Saski, S. M. Zakeeruddin, J. Lewiński, M. Grätzel, *ACS Appl. Mater. Interfaces* **2017**, *9*, 28418.
[7] Y. Zhang, Y. Wang, X. Yang, L. Zhao, R. Su, J. Wu, D. Luo, S. Li, P. Chen, M. Yu, Q. Gong, R. Zhu, *Adv. Mater.* **2022**, *34*, e2107420.
[8] W. Feng, J.-F. Liao, X. Chang, J.-X. Zhong, M. Yang, T. Tian, Y. Tan, L. Zhao, C. Zhang, B.-X. Lei, L. Wang, J. Huang, W.-Q. Wu, *Mater. Today* **2021**, *50*, 199.
[9] W. Fan, K. Deng, Y. Shen, Y. Bai, L. Li, *Angew. Chem. Int. Ed.* **2022**, *61*, e202211259.
[10] B. Dou, L. M. Wheeler, J. A. Christians, D. T. Moore, S. P. Harvey, J. J. Berry, F. S. Barnes, S. E. Shaheen, M. F. van Hest, *ACS Energy Lett.* **2018**, *3*, 979.
[11] Y. Zhang, S.-G. Kim, D.-K. Lee, N.-G. Park, *ChemSusChem* **2018**, *11*, 1813.
[12] F. Palazon, Y. El Ajjouri, H. J. Bolink, *Adv. Energy Mater.* **2019**, *48*, 1902499.

[13] Z. Hong, D. Tan, R. A. John, Y. K. E. Tay, Y. K. T. Ho, X. Zhao, T. C. Sum, N. Mathews, F. García, H. S. Soo, *iScience* **2019**, *16*, 312.
[14] a) G. E. Eperon, S. N. Habisreutinger, T. Leijtens, B. J. Bruijnaers, J. J. van Franeker, D. W. deQuilettes, S. Pathak, R. J. Sutton, G. Grancini, D. S. Ginger, R. A. J. Janssen, A. Petrozza, H. J. Snaith, *ACS Nano* **2015**, *9*, 9380; b) D. Tsvetkov, M. Mazurin, I. Ivanov, D. Malyshkin, V. Sereda, A. Zuev, *Chem. Eur. J.* **2020**, *26*, 12549.
[15] P. Fassl, V. Lami, A. Bausch, Z. Wang, M. T. Klug, H. J. Snaith, Y. Vaynzof, *Energy Environ. Sci.* **2018**, *11*, 3380.
[16] a) J. Li, J. Dagar, O. Shargaieva, M. A. Flatken, H. Köbler, M. Fenske, C. Schultz, B. Stegemann, J. Just, D. M. Többens, A. Abate, R. Munir, E. Unger, *Adv. Energy Mater.* **2021**, *11*, 2003460; b) Y. Vaynzof, *Adv. Energy Mater.* **2020**, *10*, 2003073.
[17] N. Leupold, K. Schötz, S. Cacovich, I. Bauer, M. Schultz, M. Daubinger, L. Kaiser, A. Rebai, J. Rousset, A. Köhler, P. Schulz, R. Moos, F. Panzer, *ACS Appl. Mater. Interfaces* **2019**, *11*, 30259.
[18] T. Baikie, Y. Fang, J. M. Kadro, M. Schreyer, F. Wei, S. G. Mhaisalkar, M. Graetzel, T. J. White, *J. Mater. Chem. A* **2013**, *1*, 5628.
[19] T. P. Gujar, T. Unger, A. Schönleber, M. Fried, F. Panzer, S. van Smaalen, A. Köhler, M. Thelakkat, *Phys. Chem. Chem. Phys.* **2018**, *20*, 605.
[20] a) A. M. Askar, G. M. Bernard, B. Wiltshire, K. Shankar, V. K. Michaelis, *J. Phys. Chem. C* **2017**, *121*, 1013; b) A. Senocrate, I. Moudrakovski, G. Y. Kim, T.-Y. Yang, G. Gregori, M. Grätzel, J. Maier, *Angew. Chem. Int. Ed.* **2017**, *56*, 7755.
[21] D. Liu, D. Luo, A. N. Iqbal, K. W. P. Orr, T. A. S. Doherty, Z.-H. Lu, S. D. Stranks, W. Zhang, *Nat. Mater.* **2021**, *20*, 1337.
[22] F. Palazon, Y. El Ajjouri, P. Sebastia-Luna, S. Lauciello, L. Manna, H. J. Bolink, *J. Mater. Chem. C* **2019**, *7*, 11406.
[23] a) S. Jariwala, H. Sun, G. W. Adhyaksa, A. Lof, L. A. Muscarella, B. Ehrler, E. C. Garnett, D. S. Ginger, *Joule* **2019**, *3*, 3048; b) T. W. Jones, A. Osherov, M. Alsari, M. Sponseller, B. C. Duck, Y.-K. Jung, C. Settens, F. Niroui, R. Brenes, C. V. Stan, Y. Li, M. Abdi-Jalebi, N. Tamura, J. E. Macdonald, M. Burghammer, R. H. Friend, V. Bulović, A. Walsh, G. J. Wilson, S. Lilliu, S. D. Stranks, *Energy Environ. Sci.* **2019**, *12*, 596; c) X. Xiao, W. Li, Y. Fang, Y. Liu, Y. Shao, S. Yang, J. Zhao, X. Dai, R. Zia, J. Huang, *Nat. Commun.* **2020**, *11*, 2215.
[24] a) Q. Xu, T. Eguchi, H. Nakayama, N. Nakamura, M. Kishita, *Z. Naturforsch. A* **1991**, *46*, 240; b) A. Senocrate, I. Moudrakovski, J. Maier, *Phys. Chem. Chem. Phys.* **2018**, *20*, 20043.
[25] a) M. Aebli, N. Porenta, N. Aregger, M. V. Kovalenko, *Chem. Mater.* **2021**, *33*, 6965; b) E. M. Mozur, M. A. Hope, J. C. Trowbridge, D. M. Halat, L. L. Daemen, A. E. Maughan, T. R. Prisk, C. P. Grey, J. R. Neilson, *Chem. Mater.* **2020**, *32*, 6266.
[26] T. A. S. Doherty, S. Nagane, D. J. Kubicki, Y.-K. Jung, D. N. Johnstone, A. N. Iqbal, D. Guo, K. Frohna, M. Danaie, E. M. Tennyson, S. Macpherson, A. Abfalterer, M. Anaya, Y.-H. Chiang, P. Crout, F. S. Ruggeri, S. Collins, C. P. Grey, A. Walsh, P. A. Midgley, S. D. Stranks, *Science* **2021**, *374*, 1598.
[27] a) W. M. J. Franssen, S. G. D. van Es, R. Dervişoğlu, G. A. de Wijs, A. P. M. Kentgens, *J. Phys. Chem. Lett.* **2017**, *8*, 61; b) L. Piveteau, V. Morad, M. V. Kovalenko, *J. Am. Chem. Soc.* **2020**, *142*, 19413.
[28] K. Schötz, A. M. Askar, W. Peng, D. Seeberger, T. P. Gujar, M. Thelakkat, A. Köhler, S. Huettner, O. M. Bakr, K. Shankar, F. Panzer, *J. Mater. Chem. C* **2020**, *8*, 2289.
[29] D. W. deQuilettes, K. Frohna, D. Emin, T. Kirchartz, V. Bulovic, D. S. Ginger, S. D. Stranks, *Chem. Rev.* **2019**, *119*, 11007.
[30] S. D. Stranks, V. M. Burlakov, T. Leijtens, J. M. Ball, A. Goriely, H. J. Snaith, *Phys. Rev. Appl.* **2014**, *2*, 34007.
[31] L. M. Herz, *Annu. Rev. Phys. Chem.* **2016**, *67*, 65.
[32] S.-G. Kim, J.-H. Kim, P. Ramming, Y. Zhong, K. Schötz, S. J. Kwon, S. Huettner, F. Panzer, N.-G. Park, *Nat. Commun.* **2021**, *12*, 1554.
[33] M. B. Johnston, L. M. Herz, *Acc. Chem. Res.* **2016**, *49*, 146.
[34] M. Yang, Y. Zeng, Z. Li, D. H. Kim, C.-S. Jiang, J. van de Lagemaat, K. Zhu, *Phys. Chem. Chem. Phys.* **2017**, *19*, 5043.
[35] K. V. Manukyan, A. V. Yeghishyan, D. O. Moskovskikh, J. Kapaldo, A. Mintairov, A. S. Mukasyan, *J. Mater. Sci.* **2016**, *51*, 9123.
[36] X. Liu, Y. Li, L. Zeng, X. Li, N. Chen, S. Bai, H. He, Q. Wang, C. Zhang, *Adv. Mater.* **2022**, e2108327.
[37] E. Aleksanyan, A. Aprahamian, A. S. Mukasyan, V. Harutyunyan, K. V. Manukyan, *J. Mater. Sci.* **2020**, *55*, 8665.
[38] a) I. L. Ivanov, A. S. Steparuk, M. S. Bolyachkina, D. S. Tsvetkov, A. P. Safronov, A. Zuev, *J. Chem. Thermodyn.* **2018**, *116*, 253; b) A. Senocrate, G. Y. Kim, M. Grätzel, J. Maier, *ACS Energy Lett.* **2019**, *4*, 2859.
[39] E. Gil-González, L. A. Pérez-Maqueda, P. E. Sánchez-Jiménez, A. Perejón, *J. Phys. Chem. Lett.* **2021**, *12*, 5540.

Manuscript received: November 28, 2022
Revised manuscript received: December 7, 2022
Accepted manuscript online: December 10, 2022